Code repo: github.com/sahu-lab/mem-visc
More info: sahu-lab.github.io/pubs
Dated: 4 September 2026

Molecular interfacial rheology: Lipid membrane shear viscosity Supplemental Material

Zhi-Xun Xu [†,1] and Amaresh Sahu [‡,1]

[1] *McKetta Department of Chemical Engineering, University of Texas, Austin TX 78712, USA*

This document is the supplemental material (SM) to the manuscript of the same name. In §1, we present specified and derived bilayer parameters from our simulations of both dioleoylphosphatidylcholine (DOPC) and dipalmitoylphosphatidylcholine (DPPC) membranes, as well as additional calculations. Our determination of standard errors, and methods of data fitting, are discussed in §2. The DPPC counterparts to all figures in the main text are presented in §3. Non-equilibrium molecular dynamics (NEMD) simulations are analyzed in §4, and the MD simulation methodology is provided in §5.

1. Summary of parameters and additional calculations

We begin by presenting all parameters for our DOPC and DPPC simulations in Table 1. Input files and run scripts are provided in the online repository at https://github.com/sahu-lab/mem-visc. Relevant calculations are discussed in the remainder of this section.

Table 1: Specified and derived parameters from MD simulations.

Parameter	Symbol	Units	DOPC	DPPC
lateral size	ℓ_x, ℓ_y	nm	62.48	65.05
lateral area	A	nm^2	3,904	4,232
water thickness	ℓ_z	nm	13.41	13.38
temperature	ϑ	K	298	340
number of lipids	N	–	11,776	13,312
lipid mass	m	amu	786.129	734.053
areal mass density	ρ_0	pg/nm^2	$3.938 \cdot 10^{-9}$	$3.834 \cdot 10^{-9}$
compressibility modulus	k_c	pN/nm	195	128
sound speed	c_s	nm/ps	0.222	0.183
shear viscosity	ζ	pN·µs/nm	0.184	0.064
quadratic ζ-dependence	b	nm^2	0.31	0.18

[†] zhixunxu@utexas.edu
[‡] asahu@che.utexas.edu

1.1. Membrane density and velocity fields

Let $\boldsymbol{x}_j(t)$ and $\boldsymbol{v}_j(t)$ respectively denote the in-plane position and velocity of the j^{th} lipid molecule, at the time t, in an MD simulation. Since the cross-sectional area $A = \ell_x \ell_y$ remains constant, the average areal mass density $\rho_0 = Nm/A$; here N is the total number of lipids and m is the mass of a single lipid molecule. The instantaneous density perturbation $\rho(\boldsymbol{x}, t)$ and in-plane velocity $\boldsymbol{v}(\boldsymbol{x}, t)$ are then respectively given by

$$\rho(\boldsymbol{x}, t) \,=\, \sum_{j=1}^{N} m\, \delta\big(\boldsymbol{x} - \boldsymbol{x}_j(t)\big) \,-\, \rho_0 \qquad \text{and} \qquad \boldsymbol{v}(\boldsymbol{x}, t) \,=\, \sum_{j=1}^{N} \frac{m\boldsymbol{v}_j(t)}{\rho_0}\, \delta\big(\boldsymbol{x} - \boldsymbol{x}_j(t)\big)\,. \tag{1}$$

With the Fourier decomposition $\rho(\boldsymbol{x}, t) = \sum_{\boldsymbol{q}} \hat{\rho}^{\boldsymbol{q}}(t)\, e^{i\boldsymbol{q}\cdot\boldsymbol{x}}$ and $\boldsymbol{v}(\boldsymbol{x}, t) = \sum_{\boldsymbol{q}} \hat{\boldsymbol{v}}^{\boldsymbol{q}}(t)\, e^{i\boldsymbol{q}\cdot\boldsymbol{x}}$ introduced in the main text, the Fourier coefficients are found to be given by

$$\hat{\rho}^{\boldsymbol{q}}(t) \,=\, \frac{1}{A}\int \rho(\boldsymbol{x}, t)\, e^{-i\boldsymbol{q}\cdot\boldsymbol{x}}\, \mathrm{d}A \,=\, \frac{m}{A}\sum_{j=1}^{N} e^{-i\boldsymbol{q}\cdot\boldsymbol{x}_j(t)} \tag{2}$$

and

$$\hat{\boldsymbol{v}}^{\boldsymbol{q}}(t) \,=\, \frac{1}{A}\int \boldsymbol{v}(\boldsymbol{x}, t)\, e^{-i\boldsymbol{q}\cdot\boldsymbol{x}}\, \mathrm{d}A \,=\, \frac{1}{N}\sum_{j=1}^{N} \boldsymbol{v}_j(t)\, e^{-i\boldsymbol{q}\cdot\boldsymbol{x}_j(t)}\,, \tag{3}$$

where $\mathrm{d}A := \mathrm{d}x\,\mathrm{d}y$ is an area element in the x–y plane and $\int \mathrm{d}A = A$. Given Eqs. (2) and (3), $\hat{\rho}^{\boldsymbol{q}}$ and $\hat{\boldsymbol{v}}^{\boldsymbol{q}}$ are calculated directly from the MD output.

1.2. Areal compressibility modulus

At mesoscopic scales, the membrane Helmholtz free energy is treated as an effective Hamiltonian. For an area-compressible membrane, the Hamiltonian contains a bending contribution [1–3] as well as the cost of areal compressions and dilations [2]. In our simulations, ρ_0 is chosen to be the equilibrium density (see §5), for which there is no lateral tension. For small out-of-plane and density fluctuations, the membrane Hamiltonian is given by

$$\mathcal{H} \,=\, \int \left[\frac{k_\mathrm{b}}{4}\left(\nabla_\parallel^2 h\right)^2 + \frac{k_\mathrm{c}}{2}\left(\frac{\rho}{\rho_0}\right)^2\right]\mathrm{d}A\,, \tag{4}$$

where k_b is the bending modulus and $h(\boldsymbol{x}, t)$ is the membrane height. With $h(\boldsymbol{x}, t) = \sum_{\boldsymbol{q}} \hat{h}^{\boldsymbol{q}}(t)\, e^{i\boldsymbol{q}\cdot\boldsymbol{x}}$ and the decomposition for $\rho(\boldsymbol{x}, t)$, as well as the assumption that different modes are independent, Eq. (4) can be expressed as

$$\mathcal{H} \,=\, \sum_{\boldsymbol{q}}\left(\frac{k_\mathrm{b} q^4 A}{4}\left|\hat{h}^{\boldsymbol{q}}\right|^2 + \frac{k_\mathrm{c} A}{2\rho_0^2}\left|\hat{\rho}^{\boldsymbol{q}}\right|^2\right). \tag{5}$$

By applying the equipartition theorem, we find the compressibility modulus is related to equilibrium density fluctuations according to

$$k_\mathrm{c} \,=\, \frac{\rho_0^2\, k_\mathrm{B}\vartheta}{A\,\langle|\hat{\rho}^{\boldsymbol{q}}|^2\rangle}\,. \tag{6}$$

In Eq. (6), ϑ is the absolute temperature and k_B is Boltzmann's constant. Figure 1 shows our calculation of k_c from a plot of $\langle|\hat{\rho}^{\boldsymbol{q}}|^2\rangle/\rho_0^2$ versus q.

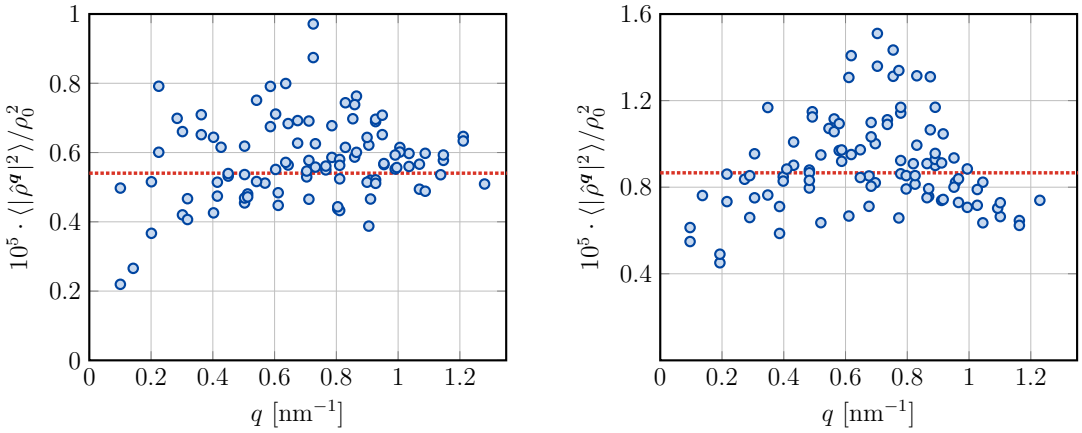

Figure 1: Fitting small-q measurements of $\langle|\hat{\rho}^{\boldsymbol{q}}|^2\rangle/\rho_0^2$ to a constant yields $k_{\mathrm{B}}\vartheta/(k_{\mathrm{c}}A)$ [cf. Eq. (6)], from which the compressibility modulus k_{c} is determined. Results for DOPC (left) and DPPC (right) are shown, with the fit using MD data for $0.2 < q < 0.6$ nm^{-1}.

1.3. Dimensional analysis of the characteristic frequency γ^q

Figure 3 of the main text shows $\gamma^q_{\mathrm{fit}} \sim q^{3/2}$. If γ^q depends only on q and the membrane parameters ζ, k_{c} , and ρ_0 entering the continuity and in-plane equations, then we seek to determine the functional dependence in $\gamma^q = \mathcal{F}(\rho_0, \zeta, k_{\mathrm{c}})\, q^{3/2}$. We recognize that $\mathcal{F}$ is a function of three parameters, and there are three independent dimensions: mass (M), length (L), and time (T). An application of dimensional analysis [4] then yields

$$\gamma^q(\rho_0, q, \zeta, k_{\mathrm{c}}) \;=\; \phi_0\, \rho_0^{\alpha}\, \zeta^{\beta}\, k_{\mathrm{c}}^{\delta}\, q^{3/2} \;, \tag{7}$$

where ϕ_0 is an unknown, $\mathcal{O}(1)$ dimensionless constant. The three exponents α , β, and δ are found by equating powers of M, L, and T on the two sides of Eq. (7). With $[\gamma] = \mathsf{T}^{-1}$, $[\rho_0] = \mathsf{M}\mathsf{L}^{-2}$, $[q] = \mathsf{L}^{-1}$, $[\zeta] = \mathsf{M}\mathsf{T}^{-1}$, and $[k_{\mathrm{c}}] = \mathsf{M}\mathsf{T}^{-2}$, we find $\alpha = {}^{-3}\!/_{4}$, $\beta = {}^{1}\!/_{2}$, and $\delta = {}^{1}\!/_{4}$. The resulting form of γ^q is presented as Eq. (4) in the main text.

2. Data fitting and error analysis

To probe the dynamics of long-wavelength modes, we simulated large systems with $\sim 10^7$ atoms (see Table 1). Our simulations on the Texas Advanced Computing Cluster generated roughly 0.7–0.9 nanoseconds of MD data per day, and so it was not feasible for us to collect data from multiple independent trajectories. All equilibrium results were generated from one 20 ns trajectory for each of the two bilayers.

2.1. The Einstein–Helfand method

As discussed in the main text, the infinite-time integral $I^{\boldsymbol{q}}_{\infty}$ cannot be reliably obtained from the running integral $I^{\boldsymbol{q}}(t)$, whose slow and noisy tail leaves the asymptote sensitive to the choice of cutoff. We instead approximate $I^{\boldsymbol{q}}_{\infty}$ from the Einstein–Helfand moment

$$G^{\boldsymbol{q}} \;:=\; \left\langle \hat{r}^{\boldsymbol{q}}_{\perp}(t)\, \hat{r}^{-\boldsymbol{q}}_{\perp}(t) \right\rangle \;, \qquad \text{where} \qquad \hat{r}^{\boldsymbol{q}}_{\perp}(t) \;:=\; \int_0^t \hat{v}^{\boldsymbol{q}}_{\perp}(t')\, \mathrm{d}t' \tag{8}$$

is the time integral of the transverse velocity [5,6]. By combining the two expressions in Eq. (8) and subsequently taking advantage of both time-translational invariance and time-reversal symmetry, we obtain

$$\begin{aligned} G^{\boldsymbol{q}}(t) &= \int_0^t \mathrm{d}t' \int_0^t \mathrm{d}t'' \left\langle \hat{v}_\perp^{\boldsymbol{q}}(t')\, \hat{v}_\perp^{-\boldsymbol{q}}(t'') \right\rangle = \int_0^t \mathrm{d}t' \int_0^t \mathrm{d}t'' \left\langle \hat{v}_\perp^{\boldsymbol{q}}(t'-t'')\, \hat{v}_\perp^{-\boldsymbol{q}}(0) \right\rangle \\ &= 2\int_0^t \mathrm{d}t' \int_0^{t'} \mathrm{d}t'' \left\langle \hat{v}_\perp^{\boldsymbol{q}}(t'-t'')\, \hat{v}_\perp^{-\boldsymbol{q}}(0) \right\rangle = 2\int_0^t \mathrm{d}t' \int_0^{t'} \mathrm{d}\tau \left\langle \hat{v}_\perp^{\boldsymbol{q}}(\tau)\, \hat{v}_\perp^{-\boldsymbol{q}}(0) \right\rangle \\ &= 2\int_0^t \mathrm{d}\tau \int_\tau^t \mathrm{d}t' \left\langle \hat{v}_\perp^{\boldsymbol{q}}(\tau)\, \hat{v}_\perp^{-\boldsymbol{q}}(0) \right\rangle = 2\int_0^t \mathrm{d}\tau \left\langle \hat{v}_\perp^{\boldsymbol{q}}(\tau)\, \hat{v}_\perp^{-\boldsymbol{q}}(0) \right\rangle \int_\tau^t \mathrm{d}t' \\ &= 2\int_0^t (t-\tau) \left\langle \hat{v}_\perp^{\boldsymbol{q}}(\tau)\, \hat{v}_\perp^{-\boldsymbol{q}}(0) \right\rangle \mathrm{d}\tau \,. \end{aligned} \tag{9}$$

Note that in the second line of Eq. (9), we change variables from t' and t'' to t' and $\tau = t' - t''$; the order of integration is swapped in going from the second line to the third line. We thus find the Einstein–Helfand moment can be expressed as

$$G^{\boldsymbol{q}}(t) = 2t \int_0^t \left\langle \hat{v}_\perp^{\boldsymbol{q}}(\tau)\, \hat{v}_\perp^{-\boldsymbol{q}}(0) \right\rangle \mathrm{d}\tau - 2\int_0^t \tau \left\langle \hat{v}_\perp^{\boldsymbol{q}}(\tau)\, \hat{v}_\perp^{-\boldsymbol{q}}(0) \right\rangle \mathrm{d}\tau \,. \tag{10}$$

At large times, the first term in Eq. (10) grows linearly in time while the second term converges to a constant, for which

$$G^{\boldsymbol{q}}(t) \sim 2t\, I_\infty^{\boldsymbol{q}} \left\langle \hat{v}_\perp^{\boldsymbol{q}}(0)\, \hat{v}_\perp^{-\boldsymbol{q}}(0) \right\rangle \qquad \text{as} \qquad t \to \infty \,. \tag{11}$$

The infinite-time integral is thus obtained from the long-time slope of $G^{\boldsymbol{q}}(t)$ divided by twice the equal-time variance $\langle \hat{v}_\perp^{\boldsymbol{q}}(0)\, \hat{v}_\perp^{-\boldsymbol{q}}(0) \rangle$. Because the slope is fit over an extended linear window, rather than read from a single point, the estimate is less sensitive to statistical noise and requires no arbitrary cutoff.

Figure 2 shows $G^{\boldsymbol{q}}(t)$ for the three wavevectors whose correlation functions appear in Fig. 2 of the main text. In each case, $G^{\boldsymbol{q}}(t)$ is approximately linear at late times; the Einstein–Helfand method is only reliable in this window. Uncertainties in the slopes are obtained with the jackknife procedure discussed below.

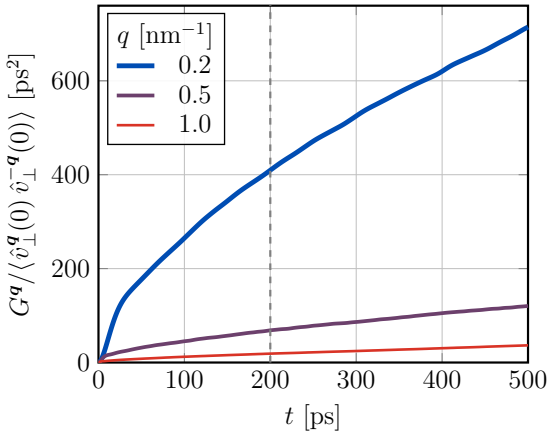

Figure 2: Einstein–Helfand moment $G^{\boldsymbol{q}}$ for a DOPC bilayer, normalized by the equilibrium velocity fluctuations $\langle \hat{v}_\perp^{\boldsymbol{q}}(0)\, \hat{v}_\perp^{-\boldsymbol{q}}(0) \rangle$ and as a function of time, for three different wavevectors. At late times, $G^{\boldsymbol{q}}(t)$ is fit to a straight line, and $I_\infty^{\boldsymbol{q}}$ is extracted from the slope.

2.2. The jackknife method

Because all equilibrium results derive from a single trajectory, we require an error estimate that (*i*) accounts for temporal correlations within one continuous time series, and (*ii*) propagates uncertainty through our analysis—namely determining the Einstein–Helfand slope, the inversion to obtain $\zeta(q)$, and the fit to $\zeta(q) = \zeta(1 - bq^2)$. We use the *delete-one block jackknife* for this purpose [7–9].

To begin, the trajectory is partitioned into n contiguous, non-overlapping blocks of equal length. Each block is long compared to the slowest relaxation time of interest, such that different blocks are statistically independent [9]. If θ denotes the quantity of interest (e.g. the membrane viscosity), the i-th jackknife replicate is formed by deleting block i and redoing the entire analysis using the remaining $n-1$ blocks; the result is expressed as $\theta_{(i)}$. The jackknife estimate of the variance of θ is given by

$$\mathrm{Var}(\theta) \;=\; \frac{n-1}{n}\sum_{i=1}^{n}\big(\theta_{(i)} - \bar{\theta}\big)^2, \qquad \text{where} \qquad \bar{\theta} \;=\; \frac{1}{n}\sum_{i=1}^{n}\theta_{(i)}\;. \tag{12}$$

and the standard error is $\mathrm{SE}(\theta) = \sqrt{\mathrm{Var}(\theta)}$. In Eq. (12), the factor of $(n-1)/n$ accounts for the small scatter among replicates, which differ only by the deletion of single blocks [8]. All error bars on $\zeta(q)$ and $I_\infty^{\boldsymbol{q}}$ in the main text, as well as the reported uncertainties in ζ and b, are one standard error as obtained from Eq. (12).

2.3. Fitting the time-dependence of transverse velocity correlation functions

As discussed in the main text, we do not know the form of the memory kernel $K^q(t)$, and so there is no predicted behavior for $C^{\boldsymbol{q}}(t)$. Through trial and error, we found the early-time behavior of the TVACF—until $t \approx 2\pi/\bar{\gamma}^q$—to be approximately given by

$$C^{\boldsymbol{q}}(t) \;\approx\; e^{-\alpha^q t}\Big(A^q\cos(\gamma^q t) + B^q\sin(\gamma^q t)\Big)\;. \tag{13}$$

Note that the damped sinusoid in Eq. (13) does not fit $C^{\boldsymbol{q}}(t)$ at very early times, and thus the four parameters are not required to satisfy the known relations $C^{\boldsymbol{q}}(0) = 1$ and $\dot{C}^{\boldsymbol{q}}(0) = 0$ [10]. We fit TVACFs over the time window $[t_{\mathrm{start}}, t_{\mathrm{end}}]$, defined as follows. Let τ_e and τ_0 respectively be the first times at which $C^{\boldsymbol{q}}(t)$ crosses $1/e$ and 0. We choose $t_{\mathrm{end}} = 3\tau_0$ when $q^2 \le 32\pi^2/\ell_x^2$ and $t_{\mathrm{end}} = 6\tau_0$ otherwise, with $t_{\mathrm{start}} = \tau_e$ in all cases. The nonlinear fit is performed with the `curve_fit` function of the `LsqFit` package in `Julia`.

3. DPPC bilayer simulations

In contrast to DOPC bilayers, DPPC membranes are not in-plane liquids at room temperature [11,12]. We thus simulate DPPC bilayers at 67° C, above the melting temperature, and reproduce plots from the main text in Fig. 3

4. Analysis of NEMD simulations

In our NEMD simulations, an in-plane body force

$$\boldsymbol{F}_j^{\mathrm{ext}} \;=\; \bar{F}\cos\big(\bar{q}\,y_j(t)\big)\,\boldsymbol{e}_x \tag{14}$$

is applied to each atom in the j^{th} lipid molecule, for all lipids. Here $y_j(t)$ is the y-component of the molecular in-plane center-of-mass $\boldsymbol{x}_j(t)$. In what follows, we connect Eq. (14) to the continuum description of the same system, solve for the nonequilibrium steady state, and show how the membrane viscosity is estimated from simulation results.

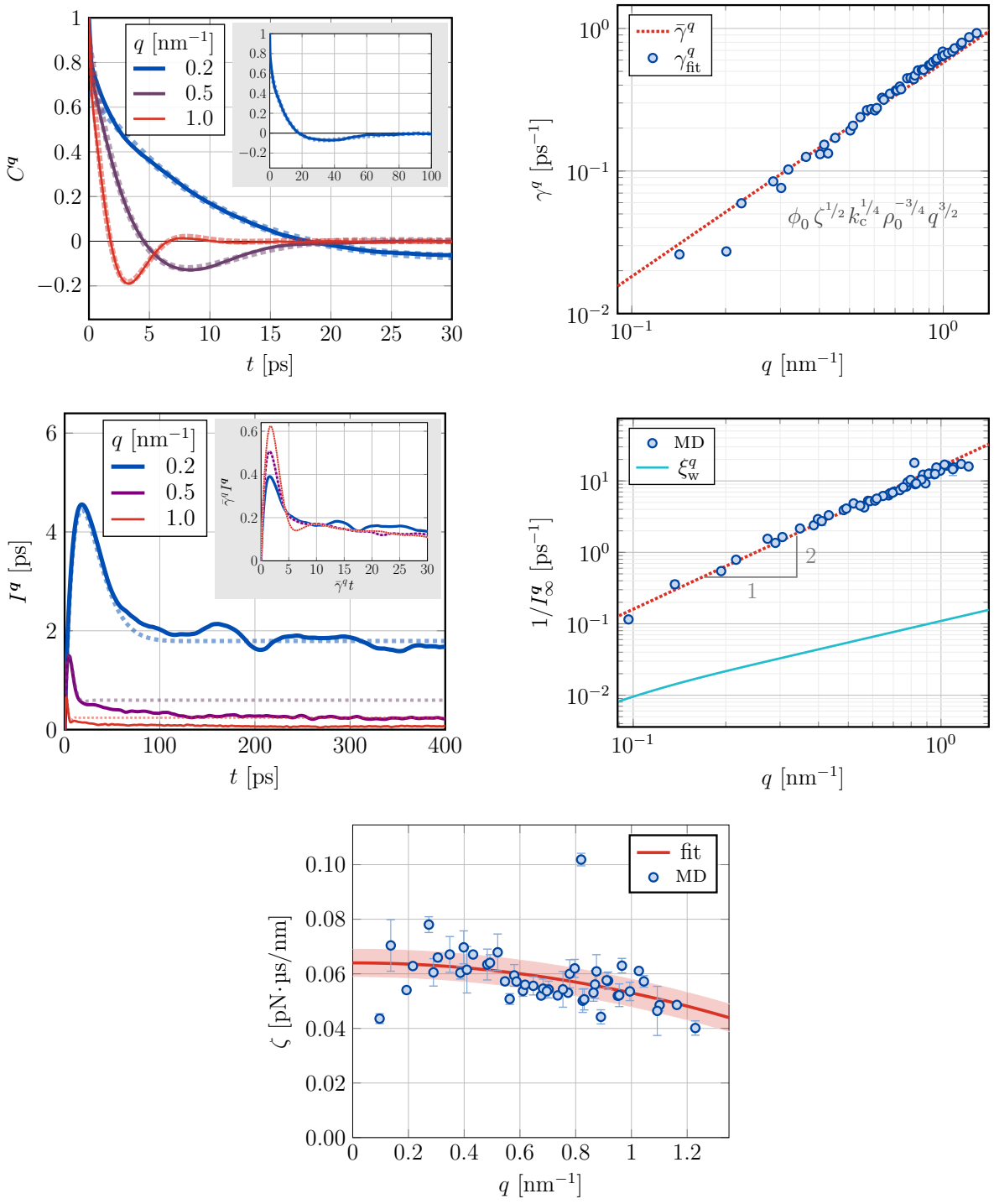

Figure 3: Results from DPPC simulations, mirroring the DOPC results from the main text. Relevant features do not show qualitative differences.

4.1. External force in the continuum equations

We begin by calculating the fluctuating, instantaneous, microscopic force per area $\boldsymbol{f}_{\mathrm{m}}^{\mathrm{ext}}$—given by

$$\boldsymbol{f}_{\mathrm{m}}^{\mathrm{ext}}(\boldsymbol{x},t) \;=\; \sum_{j=1}^{N} \boldsymbol{F}_{j}^{\mathrm{ext}}(t)\,\delta\big(\boldsymbol{x}-\boldsymbol{x}_{j}(t)\big)\;. \tag{15}$$

By substituting Eq. (14) into Eq. (15), applying properties of the Dirac δ function, rearranging terms, and then substituting Eq. (1), we find

$$\begin{aligned}
\boldsymbol{f}_{\mathrm{m}}^{\mathrm{ext}}(\boldsymbol{x},t) \;&=\; \sum_{j=1}^{N} \bar{F}\cos\big(\bar{q}\,y_{j}(t)\big)\,\boldsymbol{e}_{x}\;\delta\big(\boldsymbol{x}-\boldsymbol{x}_{j}(t)\big)\\
&=\; \sum_{j=1}^{N} \bar{F}\cos(\bar{q}y)\,\boldsymbol{e}_{x}\;\delta\big(\boldsymbol{x}-\boldsymbol{x}_{j}(t)\big)\\
&=\; \frac{\bar{F}}{m}\,\cos(\bar{q}y)\,\boldsymbol{e}_{x}\sum_{j=1}^{N} m\,\delta\big(\boldsymbol{x}-\boldsymbol{x}_{j}(t)\big)\\
&=\; \frac{\bar{F}}{m}\,\big(\rho_{0}+\rho(\boldsymbol{x},t)\big)\,\cos(\bar{q}y)\,\boldsymbol{e}_{x}\;.
\end{aligned} \tag{16}$$

In the last line of Eq. (16), the density perturbation is much smaller than the average density by construction ($|\rho| \ll \rho_{0}$), and $\rho(\boldsymbol{x},t)$ averages to zero. The external force per area $\boldsymbol{f}^{\mathrm{ext}}(\boldsymbol{x},t)$ in the continuum description is then given by

$$\boldsymbol{f}^{\mathrm{ext}}(\boldsymbol{x},t) \;=\; \frac{\bar{F}\rho_{0}}{m}\,\cos(\bar{q}y)\,\boldsymbol{e}_{x}\;. \tag{17}$$

4.2. Continuum solution to the nonequilibrium steady state

With the external force per area in Eq. (17), we seek the steady-state membrane velocity. The time-independent equations governing the membrane and fluid, to linear order, are given by

$$\begin{aligned}
&\boldsymbol{\nabla}_{\!\parallel}\cdot\bar{\boldsymbol{v}} \;=\; 0\;, \qquad && \zeta\nabla_{\!\parallel}^{2}\bar{\boldsymbol{v}} \;-\; c_{\mathrm{s}}^{2}\boldsymbol{\nabla}_{\!\parallel}\bar{\rho} \;+\; \bar{\boldsymbol{f}} \;+\; \boldsymbol{f}^{\mathrm{ext}} \;=\; 0\;,\\
&\boldsymbol{\nabla}\cdot\bar{\boldsymbol{v}}^{\pm} = 0\;, \qquad && \text{and} \qquad\quad \mu\nabla^{2}\bar{\boldsymbol{v}}^{\pm} \;-\; \boldsymbol{\nabla}\bar{p}^{\pm} \;=\; 0\;.
\end{aligned} \tag{18}$$

In Eq. (18), the 'bar' accent denotes a steady-state quantity, '$\pm$' refers to the fluid above and below the membrane, and p denotes the fluid pressure. Since the external force in Eq. (17) is only in the x-direction and has a sinusoidal dependence on y, we begin with the *ansatz* $\bar{v}_{x}^{\pm} = V^{\pm}(z)\cos(\bar{q}y)$, $\bar{v}_{y}^{\pm} = \bar{v}_{z}^{\pm} = 0$, and $\bar{p}^{\pm} = \bar{p}^{\pm}(y,z)$ in the water, as well as $\bar{v}_{x} = \bar{v}\cos(\bar{q}y)$ and $\bar{v}_{y} = 0$ in the membrane; note that the steady-state membrane continuity equation implies $\bar{\rho}$ is constant. With the no-slip conditions $\bar{v}_{x}^{\pm}(y,z=0) = \bar{v}\cos(\bar{q}y)$ and the traction-free conditions $\partial_{z}\bar{v}_{x}^{+}(y,z=\ell_{z}) = 0$ and $\partial_{z}\bar{v}_{x}^{-}(y,z=-\ell_{z}) = 0$, the system of coupled membrane and fluid equations is well-posed. In the water, we find $\bar{p}^{+}$ and $\bar{p}^{-}$ are constants, along with the velocity profile

$$\bar{v}_{x}^{\pm}(y,z) \;=\; \bar{v}\cos(\bar{q}y)\left[\frac{e^{\pm\bar{q}z}}{1+e^{2\bar{q}\ell_{z}}} \;+\; \frac{e^{\mp\bar{q}z}}{1+e^{-2\bar{q}\ell_{z}}}\right]. \tag{19}$$

It is useful to note that the fluid velocity is symmetric about $z = 0$: $\bar{v}_x^+(y,z) = \bar{v}_x^-(y,-z)$. The x-component of the traction on the membrane by the surrounding fluid, $\bar{f}_x$, is then given by

$$\bar{f}_x \;=\; 2\mu\,\frac{\partial \bar{v}_x^+}{\partial z}\bigg|_{z=0} \;=\; -2\mu\bar{v}\bar{q}\,\tanh(\bar{q}\ell_z)\cos(\bar{q}y)\;. \tag{20}$$

Substituting Eqs. (17) and (20) into the x-component of the in-plane membrane equation, Eq. $(18)_2$, yields

$$\frac{\bar{F}\rho_0}{m}\cos(\bar{q}y) \;-\; \zeta\bar{q}^2\bar{v}\cos(\bar{q}y) \;-\; 2\mu\bar{v}\bar{q}\,\tanh(\bar{q}\ell_z)\cos(\bar{q}y) \;=\; 0\;, \tag{21}$$

for which

$$\bar{v} \;=\; \frac{\bar{F}\rho_0/m}{\zeta\bar{q}^2 + 2\mu\bar{q}\tanh(\bar{q}\ell_z)} \;=\; \frac{\bar{F}}{\xi^{\bar{q}}m}\;. \tag{22}$$

4.3. Calculation of the membrane viscosity from simulation results

Equation (22) provides a relation between the magnitude of the applied force $\bar{F}$ and the resulting velocity $\bar{v}$. In NEMD simulations, we specify $\bar{F}$ and seek to determine $\langle\bar{v}\rangle_{\bar{F}}$: the magnitude of the average velocity response in the nonequilibrium steady-state. To this end, we first suppose the MD velocity is given exactly by the continuum prediction $\bar{\boldsymbol{v}}(\boldsymbol{x}) = \bar{v}\cos(\bar{q}y)\boldsymbol{e}_x$, for which

$$\int_0^{\ell_x}\!\mathrm{d}x\int_0^{\ell_y}\!\mathrm{d}y\,\Big(\bar{\boldsymbol{v}}(\boldsymbol{x})\cdot\boldsymbol{e}_x\cos(\bar{q}y)\Big) \;=\; \int_0^{\ell_x}\!\mathrm{d}x\int_0^{\ell_y}\!\mathrm{d}y\,\Big(\bar{v}\cos^2(\bar{q}y)\Big) \;=\; \frac{\bar{v}\,\ell_x\ell_y}{2}\;. \tag{23}$$

Substituting the instantaneous, microscopic velocity $\boldsymbol{v}(\boldsymbol{x},t)$ from Eq. (1) for $\bar{\boldsymbol{v}}$ into Eq. (23) and averaging over long times yields

$$\begin{aligned}
\langle\bar{v}\rangle_{\bar{F}} \;&=\; \lim_{\tau\to\infty}\frac{1}{\tau}\int_0^{\tau}\!\mathrm{d}t\,\left\{\frac{2}{\ell_x\ell_y}\int_0^{\ell_x}\!\mathrm{d}x\int_0^{\ell_y}\!\mathrm{d}y\,\Big(v_x(\boldsymbol{x},t)\cos(\bar{q}y)\Big)\right\}\\
&=\; \lim_{\tau\to\infty}\frac{1}{\tau}\int_0^{\tau}\!\mathrm{d}t\,\left\{\frac{2}{\ell_x\ell_y}\int_0^{\ell_x}\!\mathrm{d}x\int_0^{\ell_y}\!\mathrm{d}y\,\left[\sum_{j=1}^{N}\frac{mv_j^x(t)}{\rho_0}\,\delta\big(\boldsymbol{x}-\boldsymbol{x}_j(t)\big)\,\cos(\bar{q}y)\right]\right\}\\
&=\; \lim_{\tau\to\infty}\frac{1}{\tau}\int_0^{\tau}\!\mathrm{d}t\,\left\{\frac{2m}{\rho_0\,\ell_x\ell_y}\sum_{j=1}^{N}v_j^x(t)\cos\big(\bar{q}y_j(t)\big)\right\},
\end{aligned} \tag{24}$$

where in going from the second to the third lines we applied properties of the Dirac δ function. By recalling $\rho_0 = mN/A$ and $A = \ell_x\ell_y$, we obtain

$$\langle\bar{v}\rangle_{\bar{F}} \;=\; \lim_{\tau\to\infty}\frac{1}{\tau}\int_0^{\tau}\!\mathrm{d}t\,\left\{\frac{2}{N}\sum_{j=1}^{N}v_j^x(t)\,\cos\big(\bar{q}y_j(t)\big)\right\}. \tag{25}$$

In practice, we approximate $\langle\bar{v}\rangle_{\bar{F}}$ from a 1–3 ns NEMD trajectory, and look for $\langle\bar{v}\rangle_{\bar{F}}/\bar{F}$ to reach a plateau at small $\bar{F}$ (see Fig. 4). According to Eq. (22), $\xi^{\bar{q}}m$ is given by the reciprocal of the plateau value, from which we determine $\zeta^{\mathrm{NEMD}}_{\mathrm{DOPC}} = 0.26 \pm 0.01$ pN·μs/nm and $\zeta^{\mathrm{NEMD}}_{\mathrm{DPPC}} = 0.10 \pm 0.01$ pN·μs/nm.

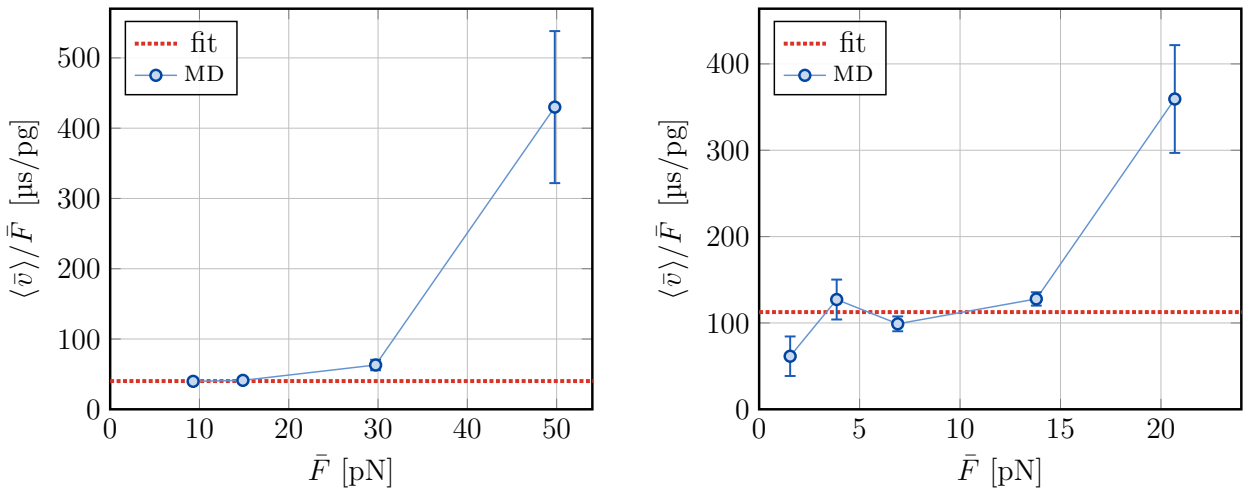

Figure 4: Results from the NEMD analysis of a DOPC bilayer (left) and a DPPC bilayer (right). The DOPC simulations reveal a clean plateau at small $\bar{F}$, while it is more difficult to find the linear regime in the case of DPPC.

5. Simulation methods

Simulations of DOPC and DPPC lipid bilayer systems were performed. For each membrane type, equilibrium simulations for calculating the shear viscosity and NEMD simulations for validation were conducted independently, respectively using `GROMACS` [13, 14] and `LAMMPS` [15]. Initial system configurations were generated via `CHARMM-GUI` [16]. The `CHARMM36m` all-atom force field was adopted for the lipids [17], and the `TIP3P` model was employed for water [18]. For all simulation scripts, see https://github.com/sahu-lab/mem-visc.

5.1. DOPC bilayer simulations

To extract the shear viscosity using `GROMACS`, initial box dimensions were 4 nm × 4 nm × 34 nm along the x-, y-, and z-directions, respectively. The system contained 46 DOPC molecules (23 in each leaflet) and 15126 `TIP3P` water molecules. All simulations employ a time step of 2 fs. Following energy minimization, an NPT equilibration was performed for 2 ns, with and periodic boundary conditions (PBCs) in all three dimensions. The system was maintained at 298 K and 1 bar using the `c-rescale` barostat. Subsequently, a shorter 200 ps NPT equilibration was performed. The configuration with the volume closest to the average volume from this trajectory was extracted and used as the initial configuration for the subsequent NVT simulation. In this NVT run, PBCs were applied in the x- and y-directions, while pseudo-walls were placed at the z boundaries. The temperature maintained at 298 K using the `v-rescale` thermostat. Walls were modeled using a Lennard-Jones 9-3 potential, which only exerts a repulsive force on water molecules in the direction perpendicular to the wall—rendering the wall–water boundary traction-free in the x- and y-directions. This equilibration was carried out for 2 ns. The equilibrated NVT configuration was subsequently replicated by a factor of 16 along each of the x- and y-directions to construct the system for the 20 ns production run.

For the NEMD simulations using `LAMMPS`, the equilibration protocol up to the NVT ensemble was identical to that employed in `GROMACS`. The equilibrated NVT configuration was then replicated by a factor of three along each of the x- and y-directions. Next, the external force defined in Eq. (14) was applied to each lipid molecule along the x-direction for 60 ps. Finally, a production simulation was carried out for 1.6 ns.

5.2. DPPC bilayer simulations

Identical protocols in GROMACS and LAMMPS were used to simulate a DPPC bilayer. The initial box dimensions were again 4 nm × 4 nm × 34 nm along the x-, y-, and z-directions, respectively. The system contained 52 DPPC molecules (26 in each leaflet) and 15424 TIP3P water molecules, with the temperature maintained at 340 K throughout the simulations.

References

[1] Canham, P. B. The minimum energy of bending as a possible explanation of the biconcave shape of the human red blood cell. *J. Theor. Biol.* **26**, 61–81 (1970).

[2] Helfrich, W. Elastic properties of lipid bilayers: Theory and possible experiments. *Z. Naturforsch. C* **28**, 693–699 (1973).

[3] Evans, E. A. Bending resistance and chemically induced moments in membrane bilayers. *Biophys. J.* **14**, 923–931 (1974).

[4] Barenblatt, G. I. *Scaling, Self-similarity, and Intermediate Asymptotics*. Cambridge Texts in Applied Mathematics (Cambridge University Press, Cambridge, 1996).

[5] Helfand, E. Transport coefficients from dissipation in a canonical ensemble. *Phys. Rev.* **119**, 1–9 (1960).

[6] Allen, M. P. & Tildesley, D. J. *Computer Simulation of Liquids* (Oxford University Press, New York, 2017), 2nd edn.

[7] Quenouille, M. H. Approximate tests of correlation in time-series. *J. R. Stat. Soc. Series B* **11**, 68–84 (1949).

[8] Efron, B. & Stein, C. The jackknife estimate of variance. *Ann. Stat.* **9**, 586–596 (1981).

[9] Flyvbjerg, H. & Petersen, H. G. Error estimates on averages of correlated data. *J. Chem. Phys.* **91**, 461–466 (1989).

[10] Hansen, J.-P. & McDonald, I. R. *Theory of Simple Liquids: With Applications to Soft Matter* (Academic Press, London, 2013), 4th edn.

[11] Koynova, R. & Caffrey, M. Phases and phase transitions of the hydrated phosphatidylethanolamines. *Chem. Phys. Lipids* **69**, 1–34 (1994).

[12] Khakbaz, P. & Klauda, J. B. Investigation of phase transitions of saturated phosphocholine lipid bilayers via molecular dynamics simulation. *Biochim. Biophys. Acta, Biomembr.* **1860**, 1489–1501 (2018).

[13] Abraham, M. J. *et al.* GROMACS: High performance molecular simulations through multi-level parallelism from laptops to supercomputers. *SoftwareX* **1-2**, 19–25 (2015).

[14] Abraham, M. *et al.* GROMACS 2024.4 source code (2024). URL https://doi.org/10.5281/zenodo.14016590.

[15] Thompson, A. P. *et al.* LAMMPS - a flexible simulation tool for particle-based materials modeling at the atomic, meso, and continuum scales. *Comp. Phys. Commun.* **271**, 108171 (2022).

[16] Feng, S., Park, S., Choi, Y. K. & Im, W. CHARMM-GUI membrane builder: Past, current, and future developments and applications. *J. Chem. Theory Comput.* **19**, 2161–2185 (2023).

[17] Klauda, J. B. *et al.* Update of the CHARMM all-atom additive force field for lipids: Validation on six lipid types. *J. Phys. Chem. B* **114**, 7830–7843 (2010).

[18] Jorgensen, W. L., Chandrasekhar, J., Madura, J. D., Impey, R. W. & Klein, M. L. Comparison of simple potential functions for simulating liquid water. *J. Chem. Phys.* **79**, 926–935 (1983).